Multipartite Entanglement Among Single Spins in Diamond

P. Neumann, *et al.*

Science **320**, 1326 (2008);
DOI: 10.1126/science.1157233

Multipartite Entanglement Among Single Spins in Diamond

P. Neumann,[1]* N. Mizuochi,[2]* F. Rempp,[1] P. Hemmer,[3] H. Watanabe,[4] S. Yamasaki,[5] V. Jacques,[1] T. Gaebel,[1] F. Jelezko,[1] J. Wrachtrup[1]†

Robust entanglement at room temperature is a necessary requirement for practical applications in quantum technology. We demonstrate the creation of bipartite- and tripartite-entangled quantum states in a small quantum register consisting of individual ^{13}C nuclei in a diamond lattice. Individual nuclear spins are controlled via their hyperfine coupling to a single electron at a nitrogen-vacancy defect center. Quantum correlations are of high quality and persist on a millisecond time scale even at room temperature, which is adequate for sophisticated quantum operations.

Schrödinger coined the term "entanglement" to mean a peculiar mutual quantum interaction in which the properties of two or more physical objects can be correlated, even when separated. Since then, the generation and retrieval of entanglement among several qubits have become of fundamental importance in quantum science and technology. Quantum teleportation error correction, computation, and communication all benefit from (or require) entanglement. One current challenge for the field of quantum information processing has been to engineer a sufficiently large and complex controllable system in which questions related to entanglement can be precisely explored. Hence, proving entanglement among an increasing number of qubits is typically a benchmark for physical systems, in demonstrating their relevance to engineer quantum states. On the level of single quantum systems, entanglement has been proven for photons (*1*), ions (*2*, *3*), atoms (*4*), and superconductors (*5*). All solid-state qubit devices require low temperature to achieve sufficiently long entanglement lifetime. Whereas single electron spins can be accessed by charge transport (*6*) or optically (*7*), nuclei are more promising for quantum engineering because of their long coherence times, even under ambient conditions. Because of their weak interaction with the environment, nuclear spins are not directly affected by (for example) lattice phonons, which are a prominent source for dephasing in most solid-state systems. In ensemble studies, (pseudo)entanglement among nuclei has been demonstrated (*8*–*10*), but this has not been confirmed for single nuclear spins so far.

For the present experiments, ^{13}C nuclei coupled to a single nitrogen-vacancy (NV) defect center in diamond (Fig. 1A) were chosen. This system allows for high-fidelity polarization and detection of single electron and nuclear spin states, even under ambient conditions (*11*–*16*). The NV center's electron spin ($S = 1$) exhibits extraordinarily slow relaxation, with a longitudinal relaxation time T_1 (i.e., the time for spontaneous transition between pure states) on the order of milliseconds (*17*). The phase memory time T_2 is found to be around 0.6 ms (*18*). Hence, this defect has been identified as a prominent candidate for engineering quantum states and quantum information processing (*19*–*22*), as well as for high-resolution magnetometry (*23*). Scalability toward larger-scale quantum registers was proposed, for example, through optical interactions between NV centers. Alternatively, probabilistic entanglement based on photonic channels can provide efficient scaling up (*24*).

The NV center is a point defect (Fig. 1A): That is, the electron spin is mostly localized at the defect site. However, about 11% of its electron spin density is distributed over the nearest-neighbor carbon atoms (*25*), mostly those at the dangling bonds caused by the vacancy. As a result, substantial hyperfine and dipolar coupling are detectable for single nuclei localized close to the defect (*26*, *27*). Here, we use such coupling (Fig. 1B) to effectively control two nuclear spins on an individual basis, and by using this technique, we are able to demonstrate entanglement of two ^{13}C nuclear spins (N_1, N_2) in the first coordination shell of the vacancy. All four maximally entangled states, namely the Bell states

$$\Phi^{\pm} = {}^{1}\!/\!_{\sqrt{2}}(|00\rangle \pm |11\rangle) \quad (1)$$

$$\Psi^{\pm} = {}^{1}\!/\!_{\sqrt{2}}(|01\rangle \pm |10\rangle) \quad (2)$$

are generated, where "0" and "1" denote the two possible nuclear spin orientations ($m_I = -1/2 \mapsto |0\rangle$, $m_I = +1/2 \mapsto |1\rangle$, $|N_1 N_2\rangle$) (Fig. 1B).

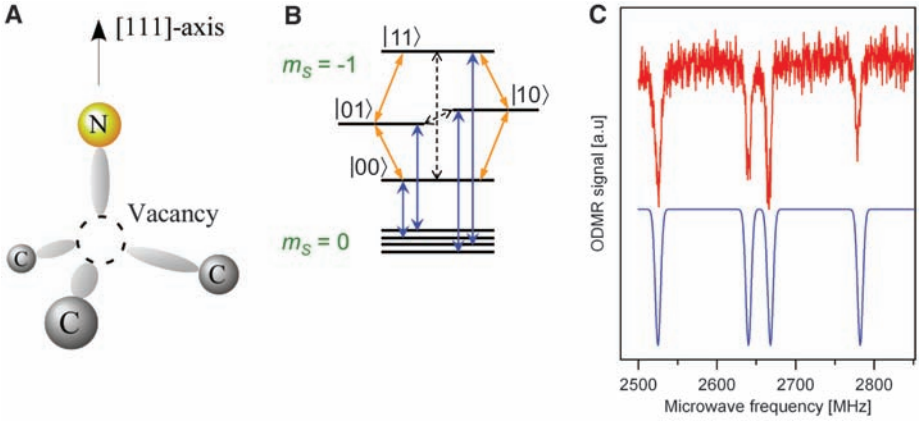

Fig. 1. (**A**) Atomic structure of the NV center. The nitrogen atom, vacancy, and three nearest-neighbor carbon atoms are shown. Two of the carbon atoms are ^{13}C isotopes with nuclear spin 1/2. (**B**) Energy-level scheme of electronic ground state of the NV center. Two of three hyperfine split electron spin sublevels ($m_S = 0, -1$) are depicted. Allowed transitions are shown by solid arrows (blue, electron spins; orange, nuclear spins). Zero and double quantum transitions are shown as dashed arrows. For further information, see (*15*). (**C**) ODMR spectrum (red curve) showing the $m_S = 0 \leftrightarrow -1$ transition. The simulated spectrum (blue curve) accounts for the hyperfine splitting of a single electron spin with two nearest-neighbor ^{13}C atoms. a.u., arbitrary units.

Table 1. Fidelity and entanglement measures for Bell, *GHZ*, and *W* states. Dashes indicate that the respective coherence measures were not calculated.

Coherence measure → Bell state ↓	Fidelity	Concurrence	Partial transpose
Ψ^+	0.80 ± 0.07	$0.65^{+0.15}_{-0.08}$	$-0.31^{+0.05}_{-0.06}$
Ψ^-	0.81 ± 0.06	0.59 ± 0.11	$-0.32^{+0.04}_{-0.05}$
Φ^+	0.98 ± 0.05	$0.96^{+0.04}_{-0.09}$	$-0.49^{+0.04}_{-0.02}$
Φ^-	0.96 ± 0.05	$0.92^{+0.07}_{-0.08}$	−0.47 ± 0.46
GHZ	0.87 ± 0.06	—	—
W	$0.85^{+0.05}_{-0.1}$	—	—

[1]3.Physikalisches Institut, Universität Stuttgart, Pfaffenwaldring 57, D-70550 Stuttgart, Germany. [2]Graduate School of Library, Information and Media Studies, University of Tsukuba, 1-2 Kasuga, Tsukuba-City, Ibaraki 305-8550, Japan. [3]Department of Electrical and Computer Engineering, Texas A&M University, College Station, TX 77843, USA. [4]Diamond Research Center, National Institute of Advanced Industrial Science and Technology (AIST), Tsukuba Central 2, Tsukuba, 305-8568, Japan. [5]Nanotechnology Research Institute AIST, Tsukuba Central 2, Tsukuba, 305-8568, Japan.

*These authors contributed equally to this work.
†To whom correspondence should be addressed. E-mail: wrachtrup@physik.uni-stuttgart.de

These entangled states cannot be achieved by independently bringing the spins into an individual superposition state: Instead, they are global states of the two spins. To demonstrate even tripartite entanglement, we take the NV center's electron spin (E) into account and generate maximally entangled states such as the Greenberger-Horne-Zeilinger (GHZ) states, as well as the so-called W state

$$GHZ = {}^{1}/_{\sqrt{2}}(|000\rangle + e^{i\varphi}|111\rangle) \quad (3)$$

$$W = {}^{1}/_{\sqrt{3}}(|110\rangle + e^{i\varphi}|101\rangle + e^{i\theta}|011\rangle) \quad (4)$$

where φ and θ are arbitrary phases. Again, "0" and "1" denote the two possible spin states of all three spins ($m_S = 0 \mapsto |0\rangle$, $m_S = -1 \mapsto |1\rangle$, $|E\,N_1N_2\rangle$).

The measured optically detected magnetic resonance (ODMR) spectrum of the electron spin of a single center is shown in Fig. 1C. Four lines separated by hyperfine splittings are observed in each $m_S = 0 \leftrightarrow -1$ and $0 \leftrightarrow 1$ transition (*15*). The Bell states $\Phi^{\pm}$ and $\Psi^{\pm}$ are prepared as follows (Fig. 2A). After initialization by optical pumping, the system is set in the $m_S = 0$ state. The nuclear spin states, however, are undetermined. To initialize a specific nuclear spin starting state, we applied a transition-selective microwave (MW) π pulse and transferred $|E\,N_1N_2\rangle = |000\rangle$ into $|100\rangle$. If the system was in $|000\rangle$ after the laser irradiation, a pure $|00\rangle$ ($=|100\rangle$) state is created. If the system was in another state after laser irradiation, a subsequent MW excitation to $|00\rangle$ does not occur, and no observable signal is visible. To increase the success rate of initialization, one can, in principle, apply additional preparation steps (*27*).

Generation of Bell states proceeds in two steps. At first, a coherent superposition of states $|01\rangle$ and $|00\rangle$ is generated with a $\pi/2$ pulse on one radio frequency (rf) transition, which yields ${}^{1}/_{\sqrt{2}}\,(|00\rangle + |01\rangle)$. By the application of a frequency-selective π pulse in resonance with the $|01\rangle$ and $|11\rangle$ transition, eventually $\Phi^- = {}^{1}/_{\sqrt{2}}\,(|00\rangle - |11\rangle)$ is formed. The remaining Bell

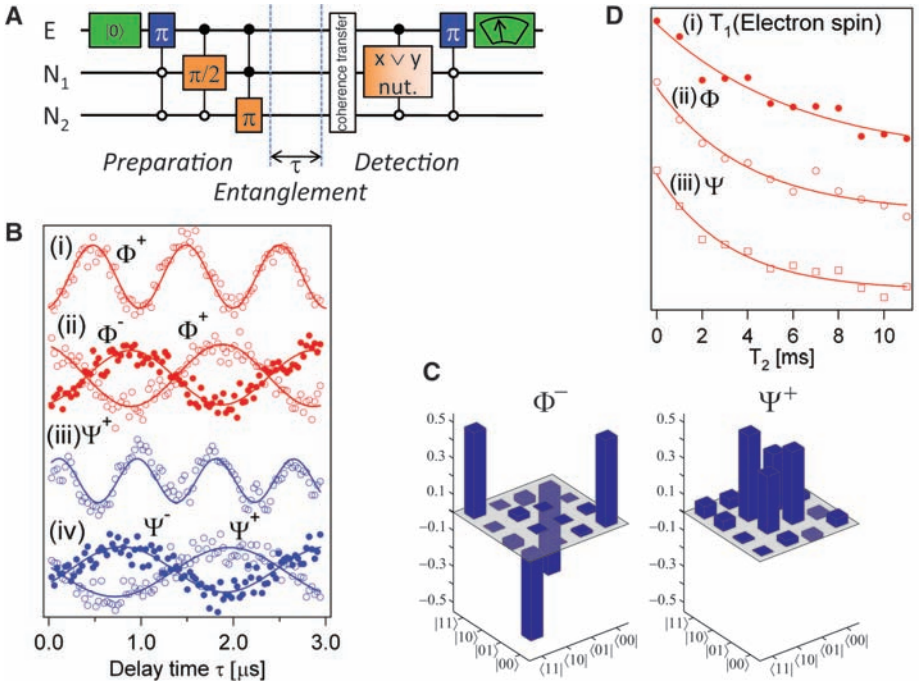

Fig. 2. (**A**) Pulse sequence for Bell state generation (Φ^-) among two nuclear spins. Spin-selective pulses are represented by squares, operating on a target qubit. Vertical lines represent logical connections. The control qubit state $|1\rangle$ and the state $|0\rangle$ are displayed as closed and open circles, respectively. For example, an open circle indicates that the pulse is applied to the target qubit if the quantum state of the controlling qubit is $|0\rangle$. Bell states evolve during time τ followed by state tomography. During six different transfer steps, the six possible coherences among the four nuclear spin states are unitarily mapped onto nuclear spin N_1. Each coherence is completely analyzed by performing two nutations (nut.) with two 90° phase-shifted rf fields. The results are the density matrix elements. (**B**) Ramsey fringes of Bell states: (i) Φ^+, (ii) Φ^+ and Φ^-, (iii) Ψ^+, and (iv) Ψ^+ and Ψ^-. The frequency offsets of rf1 ($\Delta\omega_1$), rf2 ($\Delta\omega_2$), and fitted curve (ω_{fit}) are: (i) $\Delta\omega_1 = 0.5$, $\Delta\omega_2 = 0.5$, and $\omega_{fit} = 1.0$ MHz $\approx \Delta\omega_1+\Delta\omega_2$; (ii) $\Delta\omega_1 = 0$, $\Delta\omega_2 = 0.5$, and $\omega_{fit} = 0.5$ MHz $\approx \Delta\omega_1+\Delta\omega_2$; (iii) $\Delta\omega_1 = -0.3$, $\Delta\omega_2 = 1.0$, and $\omega_{fit} = 1.3$ MHz $\approx \Delta\omega_2-\Delta\omega_1$; and (iv) $\Delta\omega_1 = 0$, $\Delta\omega_2 = 0.4$, and $\omega_{fit} = 0.4$ MHz $\approx \Delta\omega_2-\Delta\omega_1$. (**C**) Density matrix reconstruction (real part) of states Φ^- and Ψ^+. Imaginary parts are found in (*15*). The high absolute values of the main off-diagonal elements (Φ^-: $|00\rangle\langle 11|$, $|11\rangle\langle 00|$; Ψ^+: $|10\rangle\langle 01|$, $|01\rangle\langle 10|$) prove that these are, in fact, entangled states and not just incoherent mixtures (otherwise, all off-diagonal elements would be zero). (**D**) Coherence time of Bell states as compared with the relaxation time of the electron T_1.

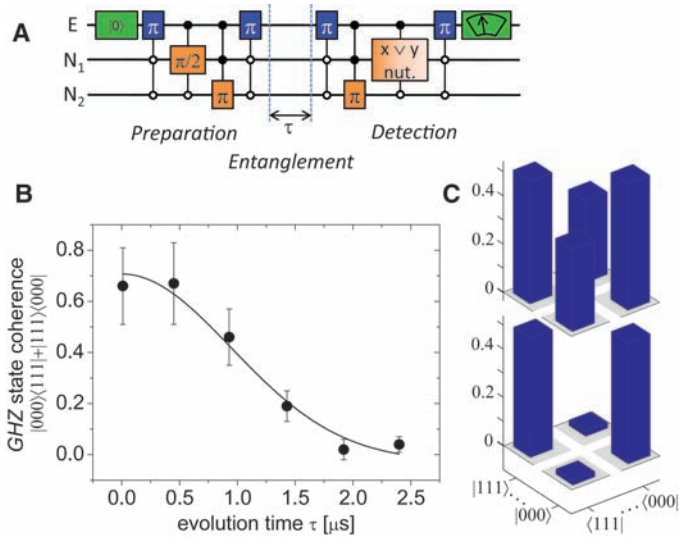

Fig. 3. (**A**) Pulse sequence for generation and detection of the GHZ state. The preparation sequence is similar to that of Bell states, followed by a selective MW pulse. For readout, a tomography is performed for the ideally nonzero density matrix elements. (**B**) Ramsey fringes of the GHZ coherence quantified by showing the sums of the respective off-diagonal elements of the density matrix ($\rho_{1,8}+\rho_{8,1} = |000\rangle\langle 111| + |111\rangle\langle 000|$). The decay is fitted to $\exp[-(\tau/T_2^*)^2]$, with $T_2^* = 1.3 \pm 0.2$ μs. Error bars indicate the accuracy of the measured data points. (**C**) Tomogram of GHZ state's main density matrix entries. Unmeasured elements are discarded. The top graph shows the density matrix for evolution time $\tau = 0$ μs, whereas the bottom graph shows the decay of off-diagonal elements for $\tau = 2.4$ μs.

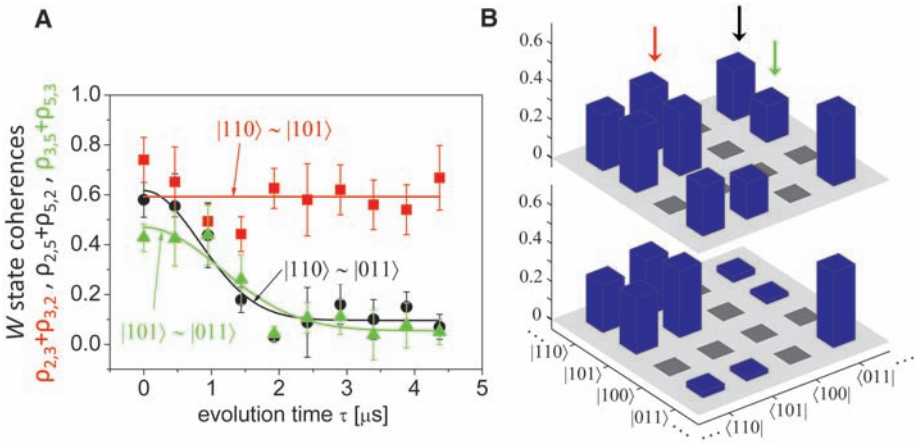

Fig. 4. (**A**) Ramsey fringes of all three coherences [sum of the corresponding off-diagonal elements: for example, $\rho_{5,2}+\rho_{2,5} = |011\rangle\langle 110| + |110\rangle\langle 011|$]. The respective off-diagonal elements are marked with a correspondingly colored arrow in (B). Only coherence between the two energy eigenstates containing the same electron spin orientation ($\rho_{3,2} = |101\rangle\langle 110|$, $\rho_{2,3} = |110\rangle\langle 101|$) shows no decay during the observation time. The others decay within 2 μs. The decay is fitted to $\exp[-(\tau/T_2^*)^2]$, with $T_2^* = 1.2 \pm 0.2$ μs for the circles and $T_2^* = 1.6 \pm 0.3$ μs for the triangles. The straight line for the squares is a guide to the eye. Error bars indicate the accuracy of the measured data points. (**B**) Tomograms of the main entries of the *W* state. The top and bottom graphs display the density matrix right after preparation and after 4.4 μs, respectively. Gray density matrix elements have not been measured.

states are prepared in a similar fashion (*28*). Having arranged the Bell states, we proved their generation via Ramsey fringes: that is, letting the Bell state evolve freely for a certain time τ and analyzing its phase afterwards (*15*). Phases of different Bell states evolve differently under rotation around the quantization axis (*28*). Φ and Ψ are characterized by an angular frequency $\Delta\omega_{\Phi,\Psi} = \Delta\omega_1+\Delta\omega_2$ and $\Delta\omega_2-\Delta\omega_1$, respectively (Fig. 2B), where $\Delta\omega_1$ and $\Delta\omega_2$ are detunings from resonance of the two radio frequency fields rf1 and rf2 involved in generation and detection of the respective Bell states. The "+" and "–" states are distinguishable by their phase with respect to the phase of the driving rf field (Fig. 2B).

A standard procedure to quantify the amount of entanglement is density matrix tomography. By measuring the probabilities to find the nuclear spins in a certain eigenstate and revealing coherent phases among them (e.g., $|00\rangle + |11\rangle$), researchers have performed density matrix tomography for all Bell states (*26*) (Fig. 2A). Tomography results are plotted in Fig. 2C. For brevity, only the real part of Φ^- and Ψ^+ is shown. Concurrence and the negative eigenvalue of the partial transpose were calculated (Table 1). To compare the measured density matrix ρ with the ideally expected one σ, we estimated the fidelity $F = \{\mathrm{tr}[(\sigma^{1/2}\rho\sigma^{1/2})^{1/2}]\}^2$ [$F = \mathrm{tr}(\sigma\rho)$ for pure states σ], where tr is the trace of a matrix. As demonstrated in Table 1, especially for $\Phi^{\pm}$, the respective values get close to ideal. It has been shown that a state ρ of two qubits is entangled if and only if its partial transpose ρ^{pt} has a negative eigenvalue (*29*, *30*). As shown in Table 1, this is indeed the case for all four states. We also have measured the coherence decay time T_2 of Φ and Ψ (Fig. 2D). Both types of Bell states decay on a time scale of 3 to 5 ms, which is similar to the relaxation time of the electron spin ($T_1 = 6$ ms).

After entangling two nuclear spins, the next step is to generate a tripartite entangled state via the electron spin of the NV center itself as the third qubit. The easiest tripartite entangled state to generate is the *GHZ* state. For its generation, we start off with a nuclear $\Phi^{\pm}$ state and apply a nuclear spin state–selective π pulse on the electron transition (Fig. 3A). For *W* state generation and further details of state preparation and readout, see (*15*). Tomography of these tripartite entangled states can be performed in a fashion similar to that of the Bell states. Note that these three spin coherences are directly observable in our spin resonance experiment. In the present work, we restricted our measurements to the main (ideally nonzero) density matrix entries of the respective entangled states (Figs. 3B and 4B). It can be shown that these elements are sufficient to calculate the fidelity $F = \mathrm{tr}(\sigma\rho)$ (*15*) (Table 1).

Because, for both states, an electron spin is now involved in the entangled states, one would expect the coherences to decay much faster than those where only nuclear spins were involved. Indeed, by measuring Ramsey fringes of *GHZ* coherence after a waiting time of 2 μs, we find that only an incoherent mixture of $|111\rangle$ and $|000\rangle$ is left (Fig. 3, B and C). The Ramsey fringe decay time is determined by inhomogeneities caused by slow spectral diffusion. Refocusing such inhomogeneities or decoupling these interactions will greatly lengthen the respective coherence time. Interaction with other spin impurities limits T_1 and T_2 of the NV center's electron spin [highest reported values: $T_1 = 380$ s, (*31*); $T_2 = 350$ μs, (*18*)]. Thus, the *GHZ* state prepared here would be an even more robust resource for quantum state engineering in a purer lattice environment.

The aforementioned *GHZ* decoherence is only expected to be due to the electron spin. This is reflected in the dephasing behavior of the *W* state. After the electron spin coherence has decayed, the remaining *W* state is written as an incoherent mixture of states $|0\rangle|11\rangle$ and $|1\rangle(|10\rangle + |01\rangle)$. Thus, for the electron spin measured to be in state $|1\rangle$, nuclear spin entanglement is expected to be found, namely the Ψ^+ nuclear spin Bell state. Observation of Ramsey fringes of all *W* state coherences indeed shows the expected behavior. The two coherences involving electron spin states decay within 2 μs, whereas the coherence with mainly nuclear spin character ($|1\rangle|\Psi^+\rangle$) persists on this time scale (Fig. 4, A and B). Nuclear spin coherence outlasts electron spin decoherence.

Given the long decoherence times found for nuclear spin entangled states, there is ample opportunity to create even higher entangled states: for example, by including the nitrogen nuclear spin that is present in the defect but which was not used here. Large-scale networks may be achieved by entangling distant defects through emitted photons. Proposals similar to this have been published (*22*). Finally, we note that *GHZ*-type spin states are ideal candidates for quantum-improved measurements. In magnetometry applications, they outperform mixed states in signal-to-noise ratio by a factor of $\sqrt{N}$, where N is the number of entangled spins (*32*). Entangled spin states in a diamond-based magnetometer thus might enhance sensitivity considerably.

References and Notes

1. J. L. O'Brien, *Science* **318**, 1567 (2007).
2. C. F. Roos *et al.*, *Phys. Rev. Lett.* **92**, 220402 (2004).
3. C. F. Roos *et al.*, *Science* **304**, 1478 (2004).
4. J. Volz *et al.*, *Phys. Rev. Lett.* **96**, 030404 (2006).
5. M. Steffen *et al.*, *Science* **313**, 1423 (2006).
6. J. M. Elzerman *et al.*, *Nature* **430**, 431 (2004).
7. J. Berezovsky *et al.*, *Science* **314**, 1916 (2006).
8. T. S. Mahesh, N. Rajendran, X. H. Peng, D. Suter, *Phys. Rev. A* **75**, 062303 (2007).
9. H. G. Krojanski, D. Suter, *Phys. Rev. Lett.* **93**, 090501 (2004).
10. L. M. K. Vandersypen *et al.*, *Nature* **414**, 883 (2001).
11. J. Harrison, M. J. Sellars, N. B. Manson, *J. Lumin.* **107**, 245 (2004).
12. A. Beveratos, R. Brouri, T. Gacoin, J. P. Poizat, P. Grangier, *Phys. Rev. A* **64**, 061802 (2001).
13. C. Kurtsiefer, S. Mayer, P. Zarda, H. Weinfurter, *Phys. Rev. Lett.* **85**, 290 (2000).
14. A. Gruber *et al.*, *Science* **276**, 2012 (1997).
15. Supporting material is available on *Science* Online.
16. L. Childress *et al.*, *Science* **314**, 281 (2006).
17. D. A. Redman, S. Brown, R. H. Sands, S. C. Rand, *Phys. Rev. Lett.* **67**, 3420 (1991).
18. T. Gaebel *et al.*, *Nat. Phys.* **2**, 408 (2006).
19. J. Wrachtrup, S. Y. Kilin, A. P. Nizovtsev, *Opt. Spectrosc.* **91**, 429 (2001).
20. L. Childress, J. M. Taylor, A. S. Sorensen, M. D. Lukin, *Phys. Rev. Lett.* **96**, 070504 (2006).
21. R. J. Epstein, F. M. Mendoza, Y. K. Kato, D. D. Awschalom, *Nat. Phys.* **1**, 94 (2005).
22. S. D. Barrett, P. Kok, *Phys. Rev. A* **71**, 060310 (2005).
23. B. M. Chernobrod, G. P. Berman, *J. Appl. Phys.* **97**, 014903 (2005).

24. L. M. Duan, R. Raussendorf, *Phys. Rev. Lett.* **95**, 080503 (2005).
25. J. H. N. Loubser, J. A. van Wyk, *Diamond Res.* **11**, 4 (1977).
26. F. Jelezko *et al.*, *Phys. Rev. Lett.* **93**, 130501 (2004).
27. M. V. G. Dutt *et al.*, *Science* **316**, 1312 (2007).
28. M. Mehring, J. Mende, W. Scherer, *Phys. Rev. Lett.* **90**, 153001 (2003).
29. A. Peres, *Phys. Rev. Lett.* **77**, 1413 (1996).
30. M. Horodecki, P. Horodecki, R. Horodecki, *Phys. Lett. A* **223**, 1 (1996).
31. J. Harrison, M. J. Sellars, N. B. Manson, *Diamond Relat. Mater.* **15**, 586 (2006).
32. V. Giovannetti, S. Lloyd, L. Maccone, *Science* **306**, 1330 (2004).

33. We acknowledge financial support by the European Union (QAP, EQUIND, and NEDQIT) and Deutsche Forschungsgemeinschaft (SFB/TR21 and the JPN-GER cooperative program). N.M. is supported by the program KAKENHI (grant no. 18740175), and V.J. is supported by the Humboldt Foundation. We thank D. Twitchen from Element Six (UK) Ltd. for providing us with ultrapure chemical vapor deposition diamond samples.

Supporting Online Material

www.sciencemag.org/cgi/content/full/320/5881/1326/DC1
Materials and Methods
Figs. S1 to S4
Tables S1 to S3
References

3 March 2008; accepted 8 May 2008
10.1126/science.1157233

Strong Dissipation Inhibits Losses and Induces Correlations in Cold Molecular Gases

N. Syassen,[1] D. M. Bauer,[1] M. Lettner,[1] T. Volz,[1]* D. Dietze,[1]† J. J. García-Ripoll,[1,2] J. I. Cirac,[1] G. Rempe,[1] S. Dürr[1]‡

Atomic quantum gases in the strong-correlation regime offer unique possibilities to explore a variety of many-body quantum phenomena. Reaching this regime has usually required both strong elastic and weak inelastic interactions because the latter produce losses. We show that strong inelastic collisions can actually inhibit particle losses and drive a system into a strongly correlated regime. Studying the dynamics of ultracold molecules in an optical lattice confined to one dimension, we show that the particle loss rate is reduced by a factor of 10. Adding a lattice along the one dimension increases the reduction to a factor of 2000. Our results open the possibility to observe exotic quantum many-body phenomena with systems that suffer from strong inelastic collisions.

Strong interactions are responsible for many interesting quantum phenomena in many-body systems: high-temperature superconductivity (*1*), excitations with fractional statistic (*2*), topological quantum computation (*3*), and a plethora of exotic behaviors in magnetic systems (*4*). One of the main physical mechanisms that gives rise to strong correlations for bosonic particles can be understood as follows. At low temperatures and for strong elastic repulsive interactions, particles tend to stay far away from each other in order to keep the energy low. That is, the wave function describing the particles tends to vanish when two of them coincide at the same position. In order to fulfill these constraints, this wave function has to be highly entangled at all times, which may give rise to counterintuitive effects both in the equilibrium properties as well as in the dynamics. In one dimension, for example, this occurs in the so-called Tonks-Girardeau gas (TGG) (*5*, *6*), where the set of allowed wave functions for bosonic particles coincide (up to some transformation) with those of free fermions. Despite being bosons, the excitation spectrum, the evolution of the density distribution, etc. correspond to those of fermionic particles. In two dimensions, the same mechanism leads to the fractional quantum Hall effect (*7*), where the ground state as well as the low energy excitations fulfill the above-mentioned constraint, giving rise to the existence of anyons, which behave neither like bosons nor fermions but have fractional statistics (*2*).

We show that inelastic interactions can be used to reach the strong correlation regime with bosonic particles: This may seem surprising because inelastic collisions are generally associated with particle losses. This behavior can be understood by using an analogy in classical optics, where light absorption is expressed by an imaginary part of the refractive index. If an electromagnetic wave impinges perpendicularly on a surface between two media with complex refractive indices n_1 and n_2, then a fraction $|(n_1 - n_2)/(n_1 + n_2)|^2$ of the intensity will be reflected. In the limit $|n_2| \to \infty$, the light is perfectly reflected off the surface, irrespective of whether n_2 is real or complex. In our case, bosons interacting with large imaginary (*8*, *9*) scattering length almost perfectly reflect off each other for an analogous reason, thereby giving rise to the same constraints in the particles' wave function as the ones corresponding to elastic collisions and thus to the same physical phenomena. In our experiment, the correlations manifest themselves in a strong suppression of the rates at which particles are lost because of inelastic collisions.

Our experiment used molecules confined to one dimension by an optical lattice, both with and without a periodic potential along the one dimension. We started with the transfer of a Bose-Einstein condensate (BEC) of ^{87}Rb atoms into a three-dimensional (3D) optical lattice in such a way that the central region of the resulting Mott insulator contains exactly two atoms at each lattice site. A Feshbach resonance at 1007.4 G (*10*) was used to associate the atom pairs to molecules (*11*). Subsequently, the magnetic field was held at 1005.5 G. Atoms remaining after the association were removed with blast light. This procedure prepared a quantum state that contains one molecule at each site of a 3D optical lattice (*12*, *13*). The optical-lattice potential seen by a molecule is $-V_\perp\cos^2(kx) - V_\perp\cos^2(ky) - V_\parallel\cos^2(kz)$, where $\lambda = 2\pi/k = 830.440$ nm is the light wavelength. At the end of the state preparation, $V_\parallel$ is equal to $V_\perp$,

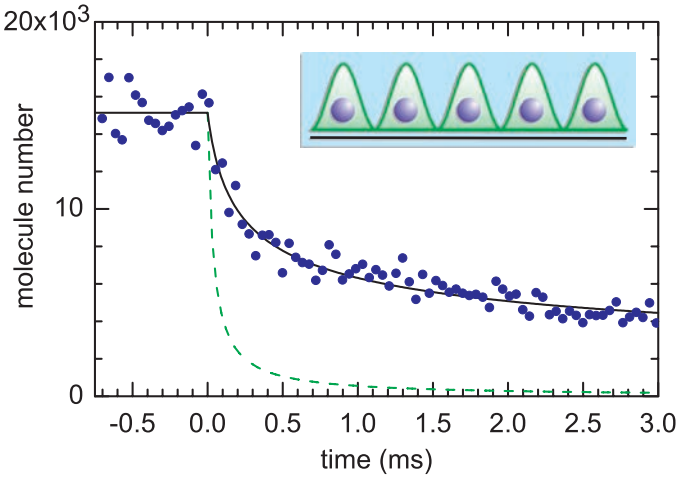

Fig. 1. Time-resolved loss of molecules at $V_\parallel = 0$. The loss begins at $t = 0$. The solid line shows a fit of Eq. 2 to the experimental data (•) with $t \leq 1$ ms. The best-fit value is $\chi n^3(0) = 4.3$/ms, corresponding to $K_{3D} = 2.2 \times 10^{-10}$ cm^3/s and, at $t = 0$, to $g^{(2)} = 0.11$. The dashed line shows the expectation for an uncorrelated system. The observed loss is much slower than the dashed line because of strong correlations.

[1]Max-Planck-Institut für Quantenoptik, Hans-Kopfermann-Straße 1, 85748 Garching, Germany. [2]Universidad Complutense, Facultad de Físicas, Ciudad Universitaria s/n, 28040 Madrid, Spain.

*Present address: Institute of Quantum Electronics, Eidgenössische Technische Hochschule (ETH)–Hönggerberg, 8093 Zürich, Switzerland.

†Present address: Institut für Photonik, Technische Universität Wien, Gußhausstraße 25-29, 1040 Wien, Austria.

‡To whom correspondence should be addressed. E-mail: stephan.duerr@mpq.mpg.de